



Strong base g-C₃N₄ with perfect structure for photocatalytically eliminating formaldehyde under visible-light irradiation

Shaoqing Song^{a,c}, Changhai Lu^c, Xi Wu^c, Shujuan Jiang^{a,c,*}, Chuanzhi Sun^{b,***}, Zhanggao Le^{c,***}

^a School of Materials Science and Chemical Engineering, Ningbo University, Ningbo 315211, PR China

^b College of Chemistry, Chemical Engineering and Materials Science, Shandong Normal University, Jinan 250014, PR China

^c State key Laboratory Breeding Base of Nuclear Resources and Environment, East China University of Technology, Nanchang 330013, PR China



ARTICLE INFO

Keyword:

Solid base photocatalyst

g-C₃N₄

π-conjugated structure

Optical and electrical properties

HCHO elimination

ABSTRACT

Solid strong base systems of g-C₃N₄ by inducing potassium (KC₃N₄) were constructed for photocatalytically decomposing HCHO. Characterization and theoretical calculation revealed that the formation of K-C and K-N perfected the π-conjugated structure of g-C₃N₄, which greatly enhanced the basicity, improve optical and electrical properties of g-C₃N₄. In the photocatalytic process, K-improved π-conjugated structure promoted HCHO adsorption, activation, completely oxidative decomposition under visible-light irradiation. Therefore, KC₃N₄ photocatalysts presented high efficiency in photocatalytic elimination of HCHO, and the optimal apparent rate reached 0.21 mol^{-0.17} L^{0.17} min⁻¹ with 1.17 reaction order by promoting the reaction between active oxygen (–OH and ·OH) and formate species under visible-light irradiation, which was 30 times of that (0.007 mol^{-0.17} L^{0.17} min⁻¹) over pristine g-C₃N₄. These results may suggest a new way for probing the advanced solid strong base photocatalysts for eliminating volatile organic compounds.

1. Introduction

People often spend more than 80% of their time in houses/apartments, offices, and cars, thus indoor air quality is crucial for human health. Formaldehyde (HCHO) is considered to be a major toxic indoor pollutant, which directly impacts on indoor air quality [1]. For improving indoor air quality, significant efforts have been made to eliminate indoor HCHO pollution, e.g., physical adsorption [2], plasma technology [3], catalytic oxidation [4–6], and photocatalytic elimination [7–9]. Visible-light responsive semiconductor-based photocatalytic elimination technology has attracted tremendous interest due to its economic, renewable, clean, and safe characteristics, and the technology has been successfully utilized to eliminate VOCs [7–17]. Inspired by polarization principle of HCHO molecular, HCHO is prone to chemical adsorption and oxidation on the electron-rich surface of catalytic materials in the presence of alkaline. Therefore, electron-rich solid base photocatalytic materials are propitious to photocatalytically oxidize and eliminate HCHO. Graphitic carbon nitride (g-C₃N₄), a π-conjugated tri-s-triazine polymer with basicity, chemical stability as well as ability of absorbing visible light with wavelength up to around 450 nm [18–20], has attracted increasing attention as a new type photocatalyst for photocatalytic poisonous pollutant elimination

[21–24], H₂O splitting [25–27], and CO₂ [28] or heavy metal ions reduction [29–31]. Under visible-light irradiation, photogenerated electrons and holes can interact with O₂ and/or H₂O to form ·O₂[–] and ·OH, which is originated from the π-conjugated structure [29]. Intuitively, g-C₃N₄ photocatalysts should be suitable for photocatalytically removing HCHO. However, g-C₃N₄ generally suffers from low efficiency, because lattice structure defects are inevitably formed in the interconnected tri-s-triazine structures of g-C₃N₄, which thus severely interfere the separation and transfer of photoinduced charge carriers. Thus, it is necessary to perfect the π-conjugated structure of g-C₃N₄ by lessening the lattice structure defects, nevertheless, the reported strategy is to only extend the π-conjugated system by grafting aromatic structures. Actually, sp²-hybridized C–N bonds in structure of g-C₃N₄ assure lone electrons on p_z orbital, which forms π-conjugated structure [32,33]. Owing to the different electronegativity between N and C, valence-electron will transfer to N [34]. When alkali metal (e.g., K) was introduced to the lattice structure of g-C₃N₄, the static coulomb between K and N–C bond will be formed by coordination between K unoccupied 3d/or 4p orbital and π-conjugated C–N p_z, which can rearrange the structure of g-C₃N₄, and lessen the effect of lattice structure defects. Moreover, K introduction will also enhance the basicity of g-C₃N₄. Logically, HCHO adsorption and activation on strong solid base g-

* Corresponding author at: School of Materials Science and Chemical Engineering, Ningbo University, Ningbo 315211, PR China.

** Corresponding authors.

E-mail addresses: jiangshujuan@nbu.edu.cn (S. Jiang), suncz@sdnu.edu.cn (C. Sun), zhgle@ecit.edu.cn (Z. Le).

C_3N_4 photocatalysts should be quite easy, which is the precondition for the subsequent HCHO dissociation.

In this paper, strong solid base KC_3N_4 photocatalysts by introducing alkali K into $\text{g-C}_3\text{N}_4$ were prepared for photocatalytic elimination of HCHO under visible-light irradiation. Experimental and theoretical investigations present that K introduction perfected the π -conjugated structure of $\text{g-C}_3\text{N}_4$, which induced strong basicity, and improved optical and electrical properties of $\text{g-C}_3\text{N}_4$. Thus the so-constructed KC_3N_4 photocatalysts demonstrated high photocatalytic performance for HCHO elimination, which was systematically elaborated in the following text.

2. Experimental

2.1. Catalyst preparation

KC_3N_4 samples were constructed via heat treatment with carbamide and KNO_3 as precursors. The specific process is as follows: 10 g carbamide was dissolved in 25 mL aqueous solution of KNO_3 and then stirred for 1.5 h. The mixed solution was dehydrated by vacuum drying at 65 °C for 2.5 h. Next, the dried and crushed samples were heated in the ceramic crucible to 540 °C by the muffle furnace for 2 h with 5 °C min⁻¹ ramp rate. After that, the yellow solid samples were obtained. The obtained samples were named as KC_3N_4 -1, KC_3N_4 -2, and KC_3N_4 -3 when the amount of KNO_3 increased from 0.20, 0.33 and 0.43 g, respectively. Meanwhile, pristine $\text{g-C}_3\text{N}_4$ was prepared by treating carbamide at 540 °C for 2 h.

2.2. Characterization

The samples were characterized by X-ray diffraction (XRD) (Bruker, D8 advance), X-ray photoelectron spectroscopy (XPS) (ESCALAB250xi, Thermo Scientific), field-emission scanning electron microscope (SEM, Hitachi), and transmission electron microscope (TEM, FEI Tecnai G20). Specific surface area and pore volume were tested on the nitrogen adsorption apparatus (Micromeritics ASAP 2020). CO_2 temperature-programmed desorption (CO_2 -TPD) was operated on FINESORB-3010 instrument. HCHO-TPD was characterized using similar method as CO_2 -TPD. Mott-Schottky plots and electrochemical impedance spectroscopy (EIS) were tested in Na_2SO_4 and KNO_3 using electrochemical workstation (CHI 660C Chenhua Instruments), respectively. Photocatalyst on glassy carbon electrode was used as working electrode. Pt, and Ag/AgCl was correspondingly utilized as counter, and reference electrode. In situ diffused Fourier transform infrared spectroscopy (In-situ DRIFT) was measured on the Thermo Fisher 6700 instrument, and photocatalyst was placed in a on-line reactor. $\cdot\text{OH}$ on KC_3N_4 was identified by photoluminescence (PL) with terephthalic acid as a probe molecule under UV illumination ($\lambda=315$ nm). Time-resolved photoluminescence spectra were recorded on FLS920 fluorescence lifetime spectrophotometer (Edinburgh, Instruments, UK). The hydroxyl radicals ($\cdot\text{OH}$) and superoxide anion radicals ($\cdot\text{O}_2^-$) were detected by electron spin resonance (ESR) with 5,5-dimethyl-1-pyrroline N-oxide (DMPO) as active-species capture agent.

2.3. Calculation

Density functional theory (DFT) calculation was performed to study the electronic structures of $\text{g-C}_3\text{N}_4$ and KC_3N_4 at the B3LYP/6-31G* standard with Gaussian 09 suite. The atomic structures of the pristine and the KC_3N_4 were modeled by a truncated unit with three melems, in which K intercalation in the defect was the optimized configuration compared to those of substitution of C or N atom. The edge C/N atoms were compensated by H to remove boundary effect. Mulliken charge distribution was collected for pristine and KC_3N_4 before and after O_2 , H_2O and HCHO adsorption.

2.4. Photocatalytic elimination of HCHO

Photocatalytic elimination of HCHO were operated in 6 L quartz photocatalytic reactor with a 5 W fan at room temperature under visible-light irradiation. A 350 W Xenon lamp was vertically placed outside the photoreactor. A UV cutoff filter (420 nm) was used to remove UV light. 0.1 g sample and 15 mL deionized H_2O was ultrasound in a culture dish (7.0 cm diameter) for 25 min to form suspension. This culture dish was dried vacuumly at 60 °C for 1 h, and a homogeneous thin film of photocatalyst was formed on the bottom of culture dish. Afterwards, this culture dish was placed into the photocatalytic reactor. A certain amount of 38% HCHO was injected into photoreactor, and the initial concentration of the evaporated HCHO after achieving the adsorption-desorption equilibrium was 300 ppm in the dark. During irradiation, HCHO, CO_2 , and H_2O concentration in the reactor was on-line conducted by a Photoacoustic IR multigas monitor (INNOVA Air Tech 95 Instruments Model 1412). The removal ratio (Y) of HCHO was calculated as $Y (\%) = (1 - C/C_0) \times 100\%$, where C and C_0 are concentrations of HCHO at 0 and t min, respectively. When the performance test was finished, the culture dish containing the photocatalyst was dried at 60 °C for 0.5 h and placed again in the reactor for the next HCHO removal reaction.

3. Results and discussion

3.1. Phase and morphology

In Fig. 1, XRD patterns of KC_3N_4 samples present the diffraction peaks of $\text{g-C}_3\text{N}_4$, i.e., (100) plane at 13.1°, and (002) plane at 27.3° [28,29], and no signals of K species was reflected due to its low concentration. It is noted that typical peaks at 13.1° and 27.3° for KC_3N_4 is slightly shifted to smaller angles. In the light of Bragg equation, interlayer spacing was increased because of K intercalation into the structure of $\text{g-C}_3\text{N}_4$, which will be in favor of preventing stacking of π -conjugated tri-s-triazine polymer nanosheet. Meanwhile, the overall peak intensity of KC_3N_4 was weakened. Owing to the distinct ionic radius, the difference of bond lengths between K, C, and N decreased the crystalline intensity of KC_3N_4 . Small-angles shift and weakened intensity of characteristic diffraction peaks preliminarily suggest K intercalation into the structure of $\text{g-C}_3\text{N}_4$, which was also confirmed by subsequent XPS characterization. C 1s and N 1s signals of KC_3N_4 samples exhibit the representative composition and structure of $\text{g-C}_3\text{N}_4$ in Fig. 1 of Supplementary Material. In K 2p signals, K 2p_{3/2} and K 2p_{1/2} peaks at 292.6 and 295.4 eV were identified, corresponding to K-N and K-C species [24], respectively, indicating intercalation of K into $\text{g-C}_3\text{N}_4$ (Fig. 1B). The K content was detected to be 0.93, 1.56–2.05 at% for KC_3N_4 -1, KC_3N_4 -2, and KC_3N_4 -3, respectively. The electron-donating property of K will affect the surface electronic states of $\text{g-C}_3\text{N}_4$, mainly reflecting the surface oxygen species. Asymmetrical O 1s peaks were presented in the XPS spectra (Fig. 1C), suggesting different oxygen species on the $\text{g-C}_3\text{N}_4$ and KC_3N_4 samples. Signals at 530.4, 532.0, and 533.0 eV are identified as the surface adsorbed oxygen (O_1), hydroxyl oxygen (O_{II}), and adsorbed H_2O molecule (O_{III}), respectively [35]. The ratio of O_{II} in surface oxygen species increased gradually with increasing K content. O_{II} will promote the conversion of formaldehyde to formic acid species, which is the important key for HCHO decomposition.

An obvious morphology change occurs for $\text{g-C}_3\text{N}_4$ after K intercalation, as shown in electron microscope observation (Fig. 1D–F). It is seen that $\text{g-C}_3\text{N}_4$ presents the accumulated nanosheets and tiny particles with irregular shape, which is representative morphology of $\text{g-C}_3\text{N}_4$ obtained by thermal polymerization. After K intercalation into the structure of $\text{g-C}_3\text{N}_4$, petal-like nanosheets with smooth and transparent features are obtained for KC_3N_4 in Fig. 1E and F. In the thermal polymerization process, K intercalation spatially prevents the accumulation of the tri-s-triazine-based two-dimensional structure; in addition, KNO_3 as a precursor can promote the combustion of outer tri-s-triazine layer

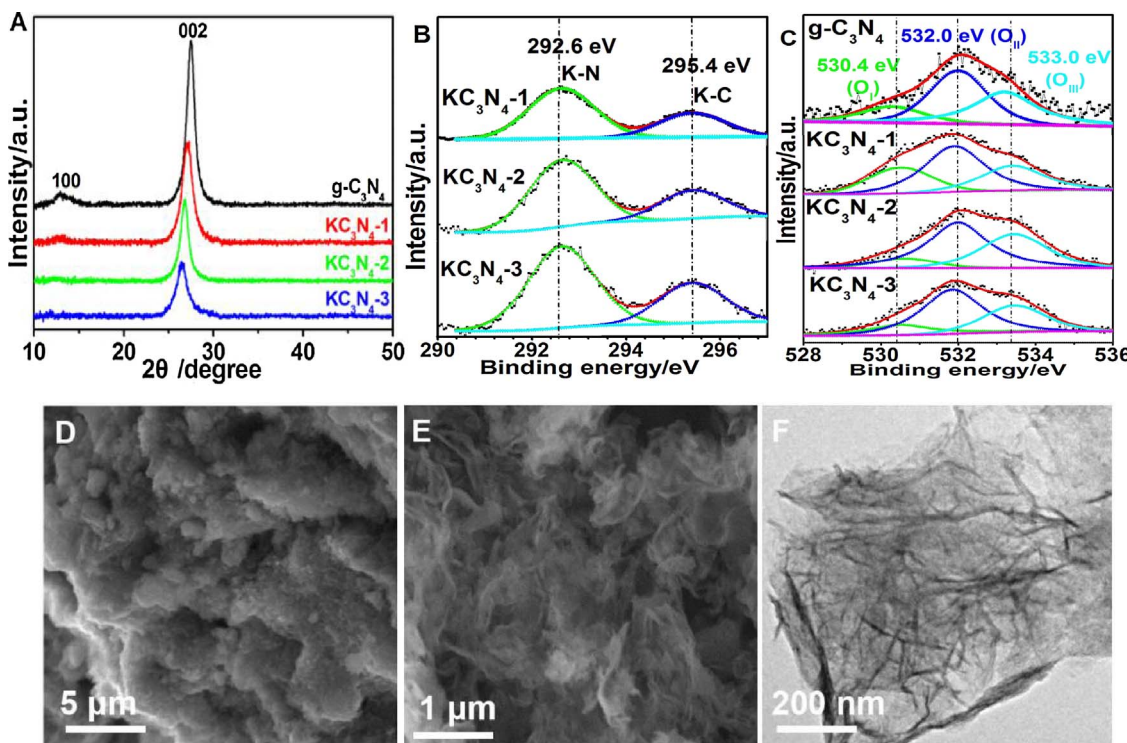


Fig. 1. XRD (A), XPS spectra for K 2p (B) and O 1 s (C), FESEM (D&E), and TEM (F) of $\text{g-C}_3\text{N}_4$ and KC_3N_4 samples. Thereinto, (D) $\text{g-C}_3\text{N}_4$, (E&F) $\text{KC}_3\text{N}_4\text{-}3$.

by releasing O_2 in the thermal treatment, therefore, KC_3N_4 samples with smooth and transparent nanosheets were obtained. The structures will effectively promote the transfer and utilization efficiency of photogenerated charge under visible-light irradiation. The N_2 adsorption/desorption isotherms and pore-size distributions indicate that KC_3N_4 samples possess mesoporous with pore size range of 10–16 nm (Fig. 2 of Supplementary Material). BET specific surface areas listed are 14, 29, 32, and $95 \text{ m}^2/\text{g}$ for $\text{g-C}_3\text{N}_4$, $\text{KC}_3\text{N}_4\text{-}1$, $\text{KC}_3\text{N}_4\text{-}2$, and $\text{KC}_3\text{N}_4\text{-}3$, respectively, and increase of surface area may arise from the decreased accumulation of the tri-s-triazine layer (Table 1 of Supplementary Material).

3.2. Surface physicochemical properties

DFT calculation was employed to investigate surface charge distribution, and adsorption behavior of $\text{g-C}_3\text{N}_4$ and KC_3N_4 . Atomic structure model of a perfect $\text{g-C}_3\text{N}_4$ consisting of melon units was supplied in Fig. 2A. Based on the result of K XPS spectra, K bonded with C and N in the optimized KC_3N_4 structure (Fig. 2B), suggesting that K was used as “atom patch” to perfect π -conjugated structure of $\text{g-C}_3\text{N}_4$. Moreover, it is obtained that surface charge of $\text{g-C}_3\text{N}_4$ is regularly distributed as listed in Fig. 2A. After introducing K, the surface of KC_3N_4 was activated reflected by the perturbed charge distribution. Consequently, the adsorption behavior of reactants on $\text{g-C}_3\text{N}_4$ and the surface basicity would be directly influenced. Adsorption energy of O_2 , H_2O , and HCHO on the surface of $\text{g-C}_3\text{N}_4$ was -12.67 , -14.18 , and 44.23 kcal/mol , respectively. Nevertheless, the corresponding adsorption energy on KC_3N_4 was greatly lowered to -40.42 , -49.55 , and -49.20 kcal/mol on or around K atom. Therefore, adsorption capability of O_2 , H_2O , and HCHO on KC_3N_4 were enhanced. Furthermore, Mulliken charge of O, H, and C atoms in these reactants on $\text{g-C}_3\text{N}_4$ and KC_3N_4 were investigated and summarized in Table 2 of Supplementary Material. Mulliken charge of O atoms in O_2 on KC_3N_4 becomes more negative (O: -0.149 ; O: -0.152) compared with those on $\text{g-C}_3\text{N}_4$ (O: 0.015 ; O: -0.009). The result reveals that electrons are more easily transferred from KC_3N_4 to O_2 , thus promoting the activation of O_2 . Mulliken charges of H_2O (O: -0.772 ; H: 0.423 ; H: 0.421) and HCHO (O:

– 0.350 ; C: 0.077) on KC_3N_4 show strong polarization compared those on $\text{g-C}_3\text{N}_4$.

Experimentally, the surface basicity and HCHO adsorption capability of $\text{g-C}_3\text{N}_4$ influenced by K intercalation was investigated by CO_2 -TPD and HCHO-TPD, respectively. In Fig. 2F, $\text{g-C}_3\text{N}_4$ sample exhibits a CO_2 desorption peak at 94°C , indicating a poor basicity of $\text{g-C}_3\text{N}_4$. K intercalation enhanced basicity of $\text{g-C}_3\text{N}_4$, as reflected the high CO_2 adsorption capability and the increased CO_2 desorption temperature [36]. In detail, large CO_2 desorption signals at $102\text{--}111^\circ\text{C}$ with a small shoulder peak centered at $412\text{--}437^\circ\text{C}$ appear in the CO_2 -TPD patterns for KC_3N_4 samples, indicating the strengthened basicity of KC_3N_4 samples. The strong basicity of KC_3N_4 samples will be in favor of HCHO adsorption in the photocatalytic elimination process, and the result was experimentally confirmed by HCHO-TPD in Fig. 4 of Supplementary Material. Therefore, charge redistribution and enhanced basicity of KC_3N_4 is conducive to adsorption and activation of O_2 , H_2O , and HCHO.

3.3. Electronic structures

DFT calculation also supplied theoretical band gap by comparing the difference between HOMO and LUMO (Table 2 of Supplementary Material), i.e., 3.8 eV ($\text{g-C}_3\text{N}_4$) and 0.55 eV (KC_3N_4), confirming that K intercalation narrowed band gap of $\text{g-C}_3\text{N}_4$ by elevating VB potential. In the UV-vis absorption spectra (Fig. 3A), $\text{g-C}_3\text{N}_4$ shows strong UV-light absorption with an absorption edge of 428 nm (Fig. 3A). On the contrary, KC_3N_4 samples exhibit enhanced visible-light absorption capability, extending the absorption boundary from 428 to 600 nm including a small absorption peak at 520 nm . The results suggest that the perfected π -conjugated structure of $\text{g-C}_3\text{N}_4$ by K introduction improve the optical and electrical properties of $\text{g-C}_3\text{N}_4$ [37]. The heightened visible-light-absorption intensity and red shift of absorption spectroscopy mean that KC_3N_4 samples can gain more solar energy to produce more photogenerated charge under visible-light irradiation. Plots of Kubelka-Munk function vs. photon energy in Fig. 3B reveal that intrinsic band-gap energy values are 2.76 , 2.47 , 2.43 , and 2.34 eV for $\text{g-C}_3\text{N}_4$, $\text{KC}_3\text{N}_4\text{-}1$, $\text{KC}_3\text{N}_4\text{-}2$, and $\text{KC}_3\text{N}_4\text{-}3$, respectively.

Electrochemical impedance spectroscopy with Mott-Schottky

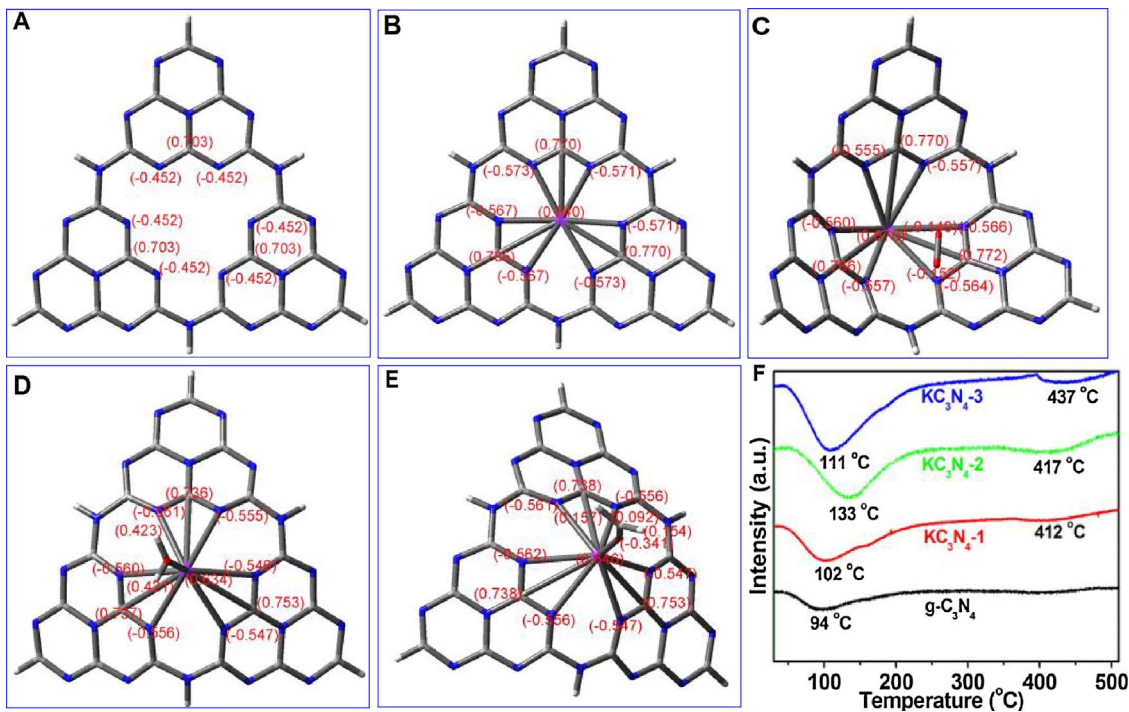


Fig. 2. Mulliken charge distribution diagrams of g-C₃N₄ (A), KC₃N₄ (B), the adsorbed O₂ (C), H₂O (D)&HCHO (E) on KC₃N₄ molecular models. (F) CO₂-TPD of g-C₃N₄ and KC₃N₄ samples.

method were shown in Fig. 3C, and it can be seen that all positive slope of tangent lines present *n*-type conductivity characteristics, and potentials of conduction band was tested to be -0.90 , -0.61 , -0.54 , and -0.34 V vs. NHE for g-C₃N₄, KC₃N₄-1, KC₃N₄-2, and KC₃N₄-3, respectively. Meanwhile, corresponding VB potentials were calculated to be 1.86 , 1.86 , 1.89 , and 2.00 V by the band gap formula (i.e., $E_g = E_{VB} - E_{CB}$). It is confirmed that both CB and VB potential increase for KC₃N₄ samples, as displayed in Fig. 3D. These results present that KC₃N₄ samples have small band-gap energy and strengthened oxidation capability of hole in VB, notably, the VB potential of KC₃N₄-3 is higher than the oxidation potential of H₂O[•]/OH. In Fig. 3E, the EIS Nyquist patterns of KC₃N₄ exhibit a gradual shrinking semicircles

compared with that of g-C₃N₄, revealing an enhanced electron-transfer capability of KC₃N₄. This result was further confirmed by the time-resolved fluorescence decay patterns. In Fig. 3F, the patterns were fitted to a biexponential decay function, and the fitting parameters were listed in Table 3 of Supplementary Material. Short lifetime (τ_1) is 0.71 , 0.85 , 0.88 , and 0.96 ns, and long lifetime (τ_2) is 4.82 , 4.95 , 5.49 , and 5.66 ns for g-C₃N₄, KC₃N₄-1, KC₃N₄-2, and KC₃N₄-3, respectively. Compared with g-C₃N₄, lifetime of charge carriers is prolonged for KC₃N₄ samples, which will heighten probability to participate in photocatalytic reactions before recombination.

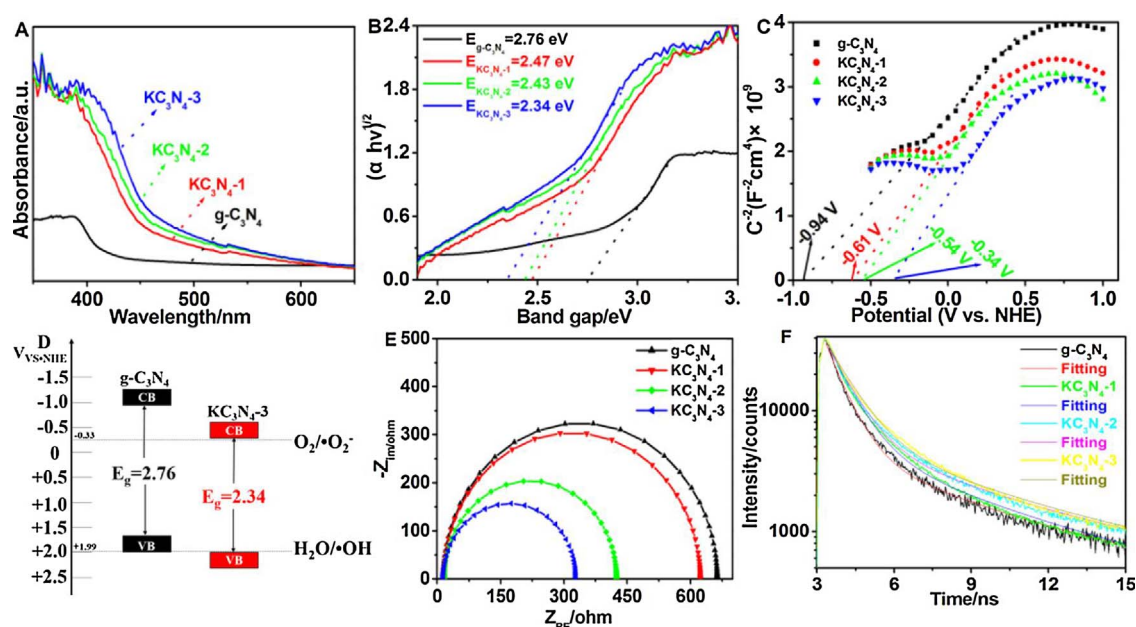
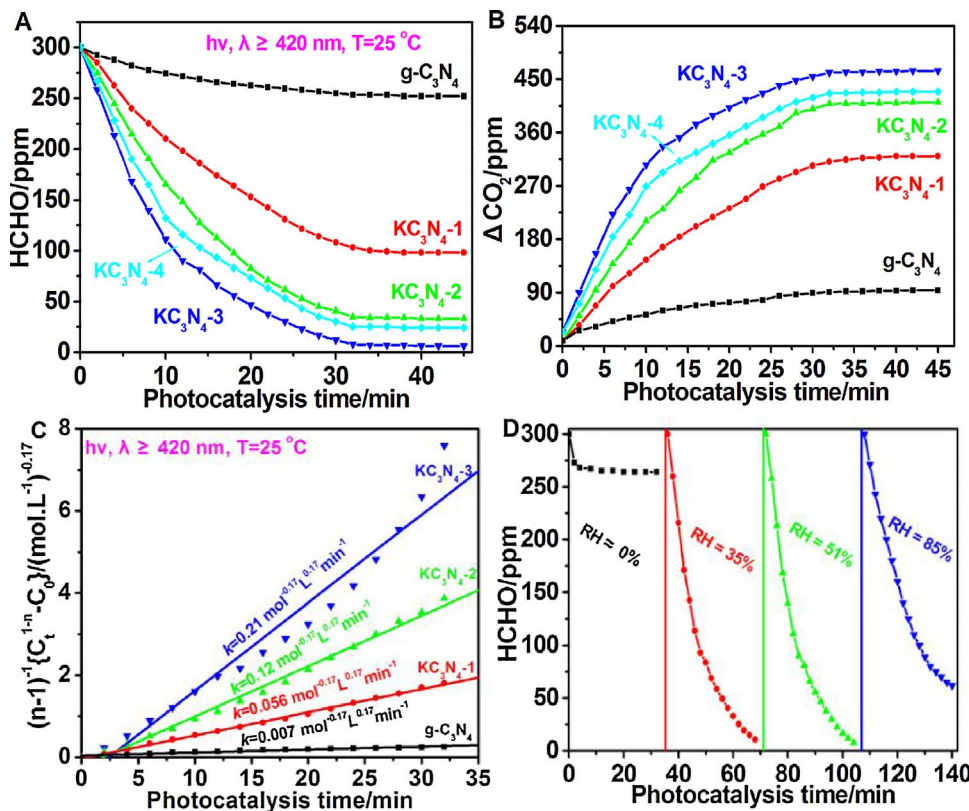


Fig. 3. UV-vis. Spectra (A), the calculated band gaps (B), Mott-Schottky plots (C), schematic illustration of band gap structure (D), EIS Nyquist plots (E), time-resolved photoluminescence spectra (F) of g-C₃N₄ and KC₃N₄ photocatalysts.



3.4. Photocatalytic performance and mechanism

Fig. 4 A presents the plots of HCHO concentration vs. irradiation time on $\text{g-C}_3\text{N}_4$ and KC_3N_4 photocatalysts at room temperature. Each experiment was carried out for 32 min, and ultimate concentration of HCHO reduced from 300 ppm to 253 ppm over $\text{g-C}_3\text{N}_4$; nevertheless, KC_3N_4 photocatalysts exhibit distinct photocatalytic activities, and HCHO concentration is 99, 34, and 7 ppm over KC_3N_4 -1, KC_3N_4 -2, and KC_3N_4 -3 after 32 min, respectively, and CO_2 concentration accordingly increases to 91, 314, 408, and 461 ppm at 32 min (Fig. 4B) over the successively elaborated photocatalysts. Moreover, the detected CO_2 concentration is higher than that from the HCHO oxidation, which mainly rises from some HCHO desorption from reactor surface in experiment process and subsequent oxidation to CO_2 , as well as the measurement accuracy of CO_2 [38,39]. Soon afterwards, no obvious enhancement was observed with increasing reaction time in Fig. 4A and B. In the whole photocatalytic process, CO was not detected. Meanwhile, we further enhanced K content of KC_3N_4 by increasing KNO_3 amount to 0.53 g in precursors, and the so-prepared sample was named as KC_3N_4 -4. In the photocatalytic elimination of HCHO, KC_3N_4 -4 nevertheless demonstrates lower activity compared with KC_3N_4 -3 in Fig. 4A and B. Thus, K introduction with suitable amount clearly promoted the photocatalytic performance of $\text{g-C}_3\text{N}_4$ for photocatalytically eliminating HCHO. Besides, we investigated photocatalytic activity over $\text{g-C}_3\text{N}_4$ and KC_3N_4 photocatalysts in the photocatalytic elimination of HCHO with 300, 350, and 400 ppm, and the photocatalytic elimination of HCHO followed 1.17-order reaction mechanism over $\text{g-C}_3\text{N}_4$ and KC_3N_4 photocatalysts (Table 4 of Supplementary Material), respectively. Therefore, the kinetic formula, i.e., $C^{1-n} - C_0^{1-n} = (n-1)kt$ ($n = 1.17$), were obtained, and subsequent reaction rate (k) in Fig. 4C is 0.007, 0.056, 0.12, and 0.21 $\text{mol}^{-0.17} \text{ L}^{0.17} \text{ min}^{-1}$ over $\text{g-C}_3\text{N}_4$, KC_3N_4 -1, KC_3N_4 -2, KC_3N_4 -3, respectively. Furthermore, KC_3N_4 -3 exhibits higher photocatalytic reactivity than other exquisitely designed photocatalytic materials and Pt-based thermal catalyst, as reflected in Table 1. As confirmed by experimental and DFT calculation results, K-

induced π -conjugated structure promotes that KC_3N_4 photocatalysts possess strong basicity, enhanced visible-light absorption, lowered band-gap energy, increased VB potential, and heightened electron-transfer capability. Strong basicity of KC_3N_4 promotes adsorption and activation of HCHO, O_2 , and H_2O . Lowered band-gap energy with enhanced visible-light absorption and improved electron-transfer capability actually impels the yield and effective utilization of photo-generated charge, and the increased VB potential is beneficial for strengthening oxidation capability of $\text{g-C}_3\text{N}_4$. Forasmuch as these characteristics KC_3N_4 photocatalysts possess, KC_3N_4 photocatalysts display high photocatalytic activity in the photocatalytic elimination of HCHO under visible-light irradiation.

Relative humidity (RH) of 30–60% in environment should be suitable for human long-term living. In consideration of the technology application, it requires researchers to probe RH effect on HCHO elimination efficiency. As can be displayed in Fig. 4D, when RH in the photocatalytic reaction system is $\approx 0\%$, HCHO concentration reduced from 300 ppm to 264 ppm for 32 min over KC_3N_4 -3, indicating that elimination efficiency is only 12%; however, HCHO elimination efficiency preserved at 96% by increasing RH to 35 and 51%. In the photocatalytic elimination of HCHO, steam did not hinder but rather accelerate HCHO elimination under visible-light irradiation. When RH further enhanced to 85%, elimination efficiency decreased to 79% due to competitive adsorption between H_2O and HCHO on the photocatalyst [40]. Furthermore, the recycles of KC_3N_4 -3 were tested at RH = 51% (Fig. 5 of Supplementary Material), and tests indicate that KC_3N_4 photocatalysts can keep a stable and efficient photocatalytic performance.

Photocatalytic elimination process of HCHO over KC_3N_4 photocatalysts was explored by in-situ DRIFT spectra (Fig. 5A). KC_3N_4 -3 photocatalyst was exposed to gaseous atmosphere of HCHO, O_2 , and H_2O , and the characteristic signals of in-situ DRIFT spectra become more distinct with reaction time. In detail, the peaks at 1265 ($\nu_s(\text{COO}^-)$), and 1438 cm^{-1} ($\nu_{as}(\text{COO}^-)$) are the typical characteristic signal of carbonate species, and peaks at 2798, 2899, and 2980 cm^{-1}

Table 1

Comparison of the HCHO elimination efficiency over KC_3N_4 -3 with the reported photocatalysts and Pt-based thermalcatalysts.

Photo-/thermal- catalysts	λ/T (nm/°C)	$[HCHO]_0$	W_{cat}	$W_{Pt}\%$	HCHO removal efficiency	Ref.
KC_3N_4 -3	$\lambda \geq 420$ nm	300 ppm	0.1 g	–	$t_{50\%} = 7$ min, $t_{90\%} = 24$ min	This work
Au/TiO_2	365 nm	50 \pm 2 ppm	N.A.	–	$t_{50\%} = 5$ min, $t_{90\%} \geq 30$ min	[7]
2D <i>p-n</i> $BiOBr/30\%BiPO_4$	400–800 nm	150 ppm	N.A.	–	$t_{50\%} = 58$ min, $t_{90\%} = 110$ min	[9]
TiMS2-550	$\lambda = 365$ nm	6.56 ppm	10 g	–	$t_{50\%} = 300$ min, $t_{90\%} \geq 660$ min	[47]
O-ZnO573	$\lambda = 400$ nm	200 ppm	0.8 g	–	$t_{50\%} = 60$ min, $t_{90\%} \geq 180$ min	[48]
$Bi_2S_3/Bi_2O_3/Bi_2O_2CO_3$	$\lambda \geq 420$ nm	500 ppm	0.1 g	–	$t_{50\%} = 45$ min, $t_{90\%} = 95$ min	[49]
$TiO_2/ACF-8h$	$\lambda = 310$ nm	0.8 ppm	0.14 g	–	$t_{50\%} = 10$ min, $t_{90\%} > 120$ min	[50]
Fe-doped WO_3	$\lambda = 458$ nm	2.4 ppm	N.A.	–	$t_{50\%} = 180$ min, $t_{90\%} > 300$ min	[51]
Ag,F,N,W-doped TiO_2	$\lambda = 420$ –470 nm	2 ppm	N.A.	–	$t_{50\%} = 43$ min, $t_{90\%} = 120$ min	[52]
$g-C_3N_4/TiO_2$	365 nm	170 \pm 10 ppm	0.3 g	–	$t_{50\%} = 13$ min, $t_{90\%} = 50$ min	[53]
0.8%Pt/Co ₃ O ₄	25 °C	210 ppm	0.1 g	0.8%	$t_{50\%} = 9$ min, $t_{90\%} = 60$ min	[58]
1%Pt/MnO ₂	23 °C	300 ppm	0.1 g	1%	$t_{50\%} = 7$ min, $t_{90\%} = 40$ min	[54]
0.8%Pt/CeO ₂ -AlOOH	25 °C	220 ppm	0.1 g	0.8%	$t_{50\%} = 10$ min, $t_{90\%} = 50$ min	[39]

Notes: λ , wavelength; T, thermal catalysis temperature; $[HCHO]_0$, initial HCHO concentration; W_{cat} , catalyst usage; $W_{Pt}\%$, percentage content of Pt; $t_{50\%}$ and $t_{90\%}$, time of 50% and 90% conversion of HCHO; Ref., reference. N.A., not available.

are considered as formate species [41]. Peaks at 1657 cm^{-1} and 3580 cm^{-1} were identified as HCHO and surface $-\text{OH}$ or H_2O , respectively [42]. The negative absorbance indicates that the adsorbed HCHO and $-\text{OH}$ or H_2O were consumed. On the one hand, the surface $-\text{OH}$ was directly reacted with HCHO, which lead to the decrease of HCHO and $-\text{OH}$, and further formed formate species; on the other, $-\text{OH}$ and/or adsorbed H_2O was transferred into intermediate active $\cdot\text{OH}$ by hole under visible-light irradiation. In Fig. 5B, PL spectra was operated to identify active oxygen species of KC_3N_4 -3 in a 5×10^{-4} M basic solution of terephthalic acid (TA) under excitation at 315 nm. Intensity of Peak at 425 nm is increasing with irradiation time, confirming $\cdot\text{OH}$ as the active oxygen species. Moreover, ESR was used to detect $\cdot\text{OH}$ and $\cdot\text{O}_2^-$ active species over photocatalysts under UV-vis light irradiation. ESR signals with the intensity ratio of 1:2:1 in Fig. 5C

can be considered as the feature of DMPO- $\cdot\text{OH}$, and intensity ratio of 1:1:1 is classified as the characteristics of DMPO- $\cdot\text{O}_2^-$ [43–45]. Consequently, we can see that $\cdot\text{OH}$ and $\cdot\text{O}_2^-$ are the main active oxygen species which take part in the photocatalysis. Therefore, in the photocatalytic elimination process, photocatalytic elimination of HCHO on KC_3N_4 photocatalysts follows a new pathway, that is, HCHO molecule was firstly adsorbed on the surface of KC_3N_4 photocatalyst with the aid of its basicity; HCHO was oxidized into formate species with the surface $-\text{OH}$ of KC_3N_4 photocatalyst; meanwhile, under visible-light irradiation, the transferred photo-induced electron from VB to CB of KC_3N_4 was trapped by O_2 to yield $\cdot\text{O}_2^-$, and $\cdot\text{O}_2^-$ reacted with H_2O to form $-\text{OH}$ [46]; Holes in VB directly oxidized $-\text{OH}$ and/or H_2O to produce $\cdot\text{OH}$, subsequently the formed formate is further oxidized to CO_2 and H_2O by $\cdot\text{OH}$, and the mechanism equation is expressed in Fig. 5C.

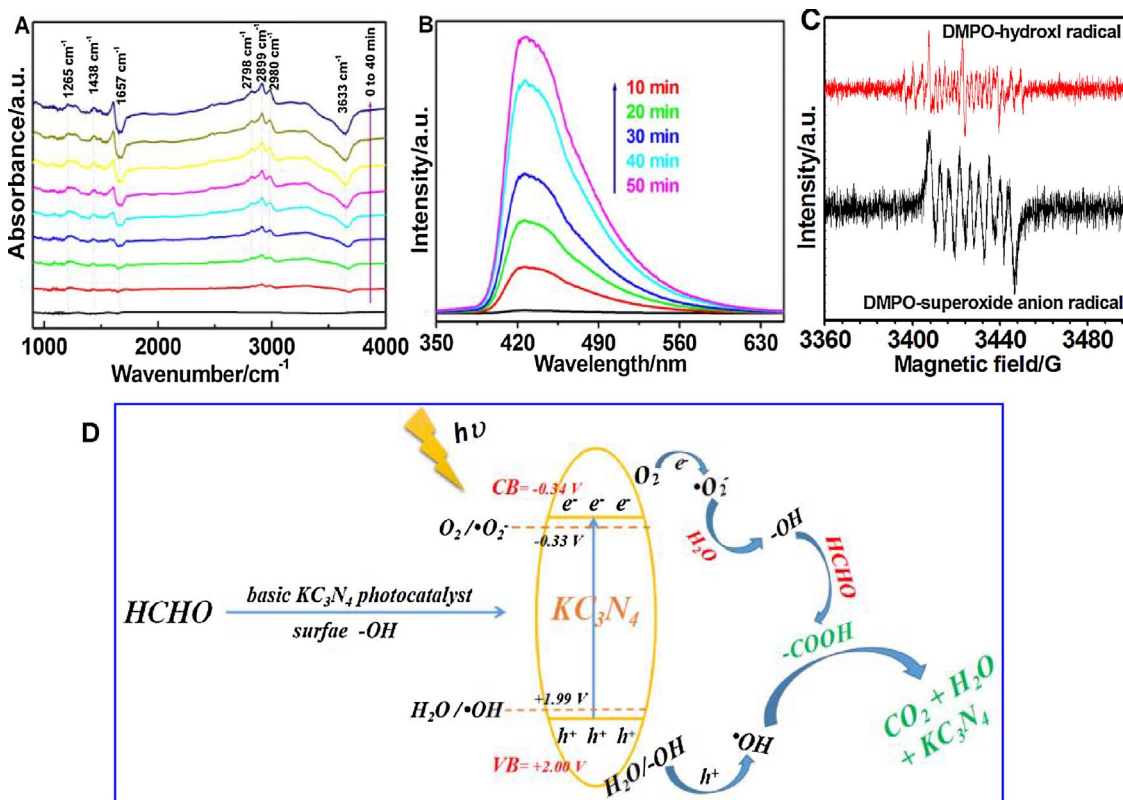


Fig. 5. In-situ DRIFTS spectra of KC_3N_4 -3 in the photocatalytic elimination process of HCHO for 40 min (A), PL spectra changes detected in the irradiation over KC_3N_4 -3 in 2×10^{-3} M NaOH solution with 5×10^{-4} M TA (B), ESR signals of DMPO - $\cdot\text{OH}$ and DMPO - $\cdot\text{O}_2^-$ for KC_3N_4 -3 under visible light irradiation (C) and the suggested mechanism for photocatalytic elimination of HCHO over KC_3N_4 photocatalyst (D).

4. Conclusion

In summary, K-induced strong base KC_3N_4 photocatalysts were constructed for HCHO oxidation under visible-light irradiation. Investigation revealed that K as “atom patch” perfected the π -conjugated structure of $\text{g-C}_3\text{N}_4$, resulting in the enhanced basicity, improved optical as well as electrical properties of $\text{g-C}_3\text{N}_4$. Thus, KC_3N_4 photocatalyst exhibited the strengthened performances of HCHO adsorption, activation, and complete decomposition under visible-light irradiation. The investigation will supply a new way for designing the advanced strong base $\text{g-C}_3\text{N}_4$ photocatalyst with perfect π -conjugated structure for the photocatalytic elimination of volatile organic compounds.

Acknowledgments

Study was supported by the National Natural Science Foundation of China (51462002, 51662003, 21667003, 21403134 and 11765002), the K. C. Wong Magna Fund in Ningbo University, and the Foundation of State key Laboratory Breeding Base of Nuclear Resources and Environment (Z201408 and Z1604).

Appendix A. Supplementary data

Supplementary data associated with this article can be found, in the online version, at <https://doi.org/10.1016/j.apcatb.2018.01.014>.

References

- J.J. Collins, R. Ness, R.W. Tyl, N. Krivanek, N.A. Esmen, T.A. Hall, A Review of adverse pregnancy outcomes and formaldehyde exposure in human and animal studies, *Regul. Toxicol. Pharmacol.* 34 (2001) 17–34.
- J.G. Yu, X.Y. Li, Z.H. Xu, W. Xiao, NaOH-modified ceramic honeycomb with enhanced formaldehyde adsorption and removal performance, *Environ. Sci. Technol.* 47 (2013) 9928–9933.
- D.Z. Zhao, X.S. Li, C. Shi, H.Y. Fan, A.M. Zhu, Low-concentration formaldehyde removal from air using a cycled storage-discharge (CSD) plasma catalytic process, *Chem. Eng. J.* 66 (2011) 3922–3929.
- S.P. Rong, P.Y. Zhang, Y.J. Yang, L. Zhu, J.L. Wang, F. Liu, MnO_2 framework for instantaneous mineralization of carcinogenic airborne formaldehyde at room temperature, *ACS Catal.* 7 (2017) 1057–1067.
- H.B. Huang, D.Y.C. Leung, Complete oxidation of formaldehyde at room temperature using TiO_2 supported metallic Pd nanoparticles, *ACS Catal.* 1 (2011) 348–354.
- P.P. Hu, Z. Amghous, Z.W. Huang, F. Xu, Y.X. Chen, X.F. Tang, Surface-confined atomic silver centers catalyzing formaldehyde oxidation, *Environ. Sci. Technol.* 49 (2015) 2384–2390.
- X.B. Zhu, C. Jin, X.S. Li, J.L. Liu, Z.G. Sun, C. Shi, X.G. Li, A.M. Zhu, Photocatalytic formaldehyde oxidation over plasmonic Au/TiO_2 under visible light: moisture indispensability and light enhancement, *ACS Catal.* 7 (2017) 6514–6524.
- X.Q. Deng, J.L. Liu, X.S. Li, X.B. Zhu, A.M. Zhu, Kinetic study on visible-light photocatalytic removal of formaldehyde from air over plasmonic Au/TiO_2 , *Catal. Today* 281 (2017) 630–635.
- Z.H. Wu, J. Liu, Q.Y. Tian, W. Wu, Efficient visible light formaldehyde oxidation with 2D *p-n* heterostructure of $\text{BiOBr}/\text{BiPO}_4$ nanosheets at room temperature, *ACS Sustainable Chem. Eng.* 5 (2017) 5008–5017.
- K. Fujiwara, Y. Kuwahara, Y. Sumida, H. Yamashita, Fabrication of photocatalytic paper Using TiO_2 nanoparticles confined in hollow silica capsules, *Langmuir* 33 (2017) 288–295.
- H.I. Kim, H.N. Kim, S. Weon, G.H. Moon, J.H. Kim, W.Y. Choi, Robust co-catalytic performance of nanodiamonds loaded on WO_3 for the decomposition of volatile organic compounds under visible light, *ACS Catal.* 6 (2016) 8350–8360.
- X.F. Qian, M. Ren, D.T. Yue, Y. Zhu, Y. Han, Z.F. Bian, Y.X. Zhao, Mesoporous TiO_2 films coated on carbon foam based on waste polyurethane for enhanced photocatalytic oxidation of VOCs, *Appl. Catal. B: Environ.* 212 (2017) 1–6.
- Y.F. Zhang, S.J. Park, Au-Pd bimetallic alloy nanoparticle-decorated BiPO_4 nanorods for enhanced photocatalytic oxidation of trichloroethylene, *J. Catal.* 355 (2017) 1–10.
- X.F. Qian, M. Ren, D.T. Yue, Y. Zhu, Y. Han, Z.F. Bian, Y.X. Zhao, Mesoporous TiO_2 films coated on carbon foam based on waste polyurethane for enhanced photocatalytic oxidation of VOCs, *Appl. Catal. B: Environ.* 212 (2017) 1–6.
- S.H. Weon, W.Y. Choi, TiO_2 nanotubes with open channels as deactivation-resistant photocatalyst for the degradation of volatile organic compounds, *Environ. Sci. Technol.* 50 (2016) 2556–2563.
- J.Z. Lyu, J.X. Gao, M. Zhang, Q. Fu, L.N. Sun, S. Hu, J.B. Zhong, S. Wang, J. Li, Construction of homojunction-adsorption layer on anatase TiO_2 to improve photocatalytic mineralization of volatile organic compounds, *Appl. Catal. B: Environ.* 202 (2017) 664–670.
- T.D. Pham, B.K. Lee, Selective removal of polar VOCs by novel photocatalytic activity of metals co-doped TiO_2/PU under visible light, *Chem. Eng. J.* 307 (2017) 63–73.
- L.P. Yang, G.H. Dong, D.L. Jacobs, Y.H. Wang, L. Zang, C.Y. Wang, Two-channel photocatalytic production of H_2O_2 over $\text{g-C}_3\text{N}_4$ nanosheets modified with perylene imides, *J. Catal.* 352 (2017) 274–281.
- J.M. Luo, G.H. Dong, Y.Q. Zhu, Z. Yang, C.Y. Wang, Switching of semiconducting behavior from n-type to p-type induced high photocatalytic NO removal activity in $\text{g-C}_3\text{N}_4$, *Appl. Catal. B: Environ.* 214 (2017) 46–56.
- G.H. Dong, D.L. Jacobs, L. Zang, C.Y. Wang, Carbon vacancy regulated photo-reduction of NO to N_2 over ultrathin $\text{g-C}_3\text{N}_4$ nanosheets, *Appl. Catal. B: Environ.* 218 (2017) 515–524.
- X. Wu, C.H. Lu, J.J. Liu, S.Q. Song, C.Z. Sun, Constructing efficient solar light photocatalytic system with Ag-introduced carbon nitride for organic pollutant elimination, *Appl. Catal. B: Environ.* 217 (2017) 232–240.
- J. Xu, Z.P. Wang, Y.F. Zhu, Enhanced visible-light-driven photocatalytic disinfection performance and organic pollutant degradation activity of porous $\text{g-C}_3\text{N}_4$ nanosheets, *ACS Appl. Mater. Interfaces* 9 (2017) 27727–27735.
- Z.X. Yu, F. Li, Q.B. Yang, H. Shi, Q. Chen, M. Xu, Nature-mimic method to fabricate polydopamine/graphitic carbon nitride for enhancing photocatalytic degradation performance, *ACS Sustainable Chem. Eng.* 5 (2017) 7840–7850.
- T. Xiong, W.L. Cen, Y.X. Zhang, F. Dong, Bridging the $\text{g-C}_3\text{N}_4$ interlayers for enhanced photocatalysis, *ACS Catal.* 6 (2016) 2462–2472.
- S.E. Guo, Y.Q. Tang, Y. Xie, C.G. Tian, Q.M. Feng, W. Zhou, B.J. Jiang, P-doped tubular $\text{g-C}_3\text{N}_4$ with surface carbon defects: universal synthesis and enhanced visible-light photocatalytic hydrogen production, *Appl. Catal. B: Environ.* 218 (2017) 664–671.
- B. Lin, H. An, X.Q. Yan, T.X. Zhang, J.J. Wei, G.D. Yang, Fish-scale structured $\text{g-C}_3\text{N}_4$ nanosheet with unusual spatial electron transfer property for high-efficiency photocatalytic hydrogen evolution, *Appl. Catal. B: Environ.* 210 (2017) 173–183.
- Q.L. Xu, B. Cheng, J.G. Yu, G. Liu, Making co-condensed amorphous carbon/ $\text{g-C}_3\text{N}_4$ composites with improved visible-light photocatalytic H_2 -production performance using Pt as cocatalyst, *Carbon* 118 (2017) 241–249.
- J.S. Wang, C.L. Qin, H.J. Wang, M.N. Chu, A. Zada, X.L. Zhang, J.D. Li, F. Raziq, Y. Qu, L.Q. Jing, Exceptional photocatalytic activities for CO_2 conversion on Al-O bridged $\text{g-C}_3\text{N}_4/\alpha\text{-Fe}_2\text{O}_3$ z-scheme nanocomposites and mechanism insight with isotopesZ, *Appl. Catal. B: Environ.* 221 (2018) 459–466.
- C.H. Lu, P. Zhang, S.J. Jiang, X. Wu, S.Q. Song, M.S. Zhu, Z.Z. Lou, Z. Li, F. Liu, Y.H. Liu, Y. Wang, Z.G. Le, Photocatalytic reduction elimination of UO_2^{2+} pollutant under visible light with metal-free sulfur doped $\text{g-C}_3\text{N}_4$ photocatalyst, *Appl. Catal. B: Environ.* 200 (2017) 378–385.
- L. Ke, P.F. Li, X. Wu, S.J. Jiang, M.B. Luo, Y.H. Liu, Z.G. Le, C.Z. Sun, S.Q. Song, Graphene-like sulfur-doped $\text{g-C}_3\text{N}_4$ for photocatalytic reduction elimination of UO_2^{2+} under visible light, *Appl. Catal. B: Environ.* 205 (2017) 319–326.
- X. Wang, M.Z. Hong, F.W. Zhang, Z.Y. Zhuang, Y. Yu, Recyclable nanoscale zero valent iron doped $\text{g-C}_3\text{N}_4/\text{MoS}_2$ for efficient photocatalysis of RhB and Cr(VI) driven by visible light, *ACS Sustainable Chem. Eng.* 4 (2016) 4055–4063.
- W.J. Ong, L.L. Tan, Y.H. Ng, S.T. Yong, S.P. Chai, Graphitic carbon nitride ($\text{g-C}_3\text{N}_4$)-based photocatalysts for artificial photosynthesis and environmental remediation: are we a step closer to achieving sustainability? *Chem. Rev.* 116 (2016) 7159–7329.
- B.C. Zhu, L.Y. Zhang, B. Cheng, J.G. Yu, First-principle calculation study of tri-s-triazine-based $\text{g-C}_3\text{N}_4$: A review, *Appl. Catal. B: Environ.* 224 (2018) 983–999.
- X.C. Wang, K. Maeda, A. Thomas, K. Takanabe, G. Xin, J.M. Carlson, K. Domon, M. Antonietti, A metal-free polymeric photocatalyst for hydrogen production from water under visible light, *Nat. Mater.* 8 (2009) 76–80.
- S.J. Jiang, E. Storr-Handberg, F. Liu, Y.T. Liao, H.Y. Wang, Z. Li, S.Q. Song, Effect of doping the nitrogen into carbon nanotubes on the activity of NiO catalysts for the oxidation removal of toluene, *Appl. Catal. B: Environ.* 160–161 (2014) 716–721.
- L.B. Sun, L. Gong, X.Q. Liu, F.N. Gu, Y. Chun, J.H. Zhu, Generating basic sites on zeolite Y by potassium species modification: effect of base precursor, *Catal. Lett.* 132 (2009) 218–224.
- M. Zhang, W.Q. Yao, Y.H. Lv, X.J. Bai, Y.F. Liu, W.J. Jiang, Y.F. Zhu, Enhancement of mineralization ability of C_3N_4 via a lower valence position by a tetra-cyanoquinodimethane organic semiconductor, *J. Mater. Chem. A* 2 (2014) 11432–11438.
- Z.X. Yan, Z.H. Xu, B. Cheng, C.J. Jiang, Co_3O_4 nanorod-supported Pt with enhanced performance for catalytic HCHO oxidation at room temperature, *Appl. Surface Sci.* 404 (2017) 426–434.
- Z.Y. Yan, Z.H. Xu, J.G. Yu, M. Jaroniec, Enhanced formaldehyde oxidation on $\text{CeO}_2/\text{AlOOH}$ -supported Pt catalyst at room temperature, *Appl. Catal. B: Environ.* 199 (2016) 458–465.
- X.B. Zhu, D.L. Chang, X.S. Li, Z.G. Sun, X.Q. Deng, A.M. Zhu, Inherent rate constants and humidity impact factors of anatase TiO_2 film in photocatalytic removal of formaldehyde from air, *Chem. Eng. J.* 279 (2015) 897–903.
- C.B. Zhang, F.D. Liu, Y.P. Zhai, H. Ariga, N. Yi, Y.C. Liu, A. Aiyotaka, M. Flytzani-Stephanopoulos, H. He, Alkali-metal-promoted Pt/ TiO_2 opens a more efficient pathway to formaldehyde oxidation at ambient temperatures, *Angew. Chem. Int. Ed.* 51 (2012) 1–6.
- P.F. Xia, B.C. Zhu, J.G. Yu, S.W. Cao, M. Jaroniec, Ultra-thin nanosheet assemblies of graphitic carbon nitride for enhanced photocatalytic CO_2 reduction, *J. Mater. Chem. A* 5 (2017) 3230–3238.
- J.J. Kong, Z.B. Rui, H.B. Ji, Carbon nitride polymer sensitization and nitrogen doping of $\text{SrTiO}_3/\text{TiO}_2$ nanotube heterostructure toward high visible light photocatalytic performance, *Ind. Eng. Chem. Res.* 56 (2017) 9999–10008.
- J.D. Xiao, J. Rabeah, J. Yang, Y.B. Xie, H.B. Cao, A. Bruckner, Fast electron transfer and OH formation: key features for high activity in visible-light-driven ozonation

with C_3N_4 catalysts, *ACS Catal.* 7 (2017) 6198–6206.

[45] M.C. Yin, Z.S. Li, J.H. Kou, Z.G. Zou, Mechanism investigation of visible light-induced degradation in a heterogeneous TiO_2 /eosin Y/rhodamine B system, *Environ. Sci. Technol.* 43 (2009) 8361–8366.

[46] M. Sayed, P.F. Fu, L.A. Shah, H.M. Khan, J. Nisar, M. Ismail, P.Y. Zhang, VUV-photocatalytic degradation of bezafibrate by hydrothermally synthesized enhanced {001} facets TiO_2 /Ti film, *J. Phys. Chem. A* 120 (2016) 118–127.

[47] R.R. Liu, J. Wang, J.J. Zhang, S. Xie, X.Y. Wang, Z.J. Ji, Honeycomb-like micro-mesoporous structure TiO_2 /sepiolite composite for combined chemisorption and photocatalytic elimination of formaldehyde, *Micropor. Mesopor. Mater.* 248 (2017) 234–245.

[48] Y.W. Tang, H. Zhou, K. Zhang, J. Ding, Y.X. Fan, D. Zhang, Visible-light-active ZnO via oxygen vacancy manipulation for efficient formaldehyde photodegradation, *Chem. Eng. J.* 262 (2015) 260–267.

[49] Y.C. Huang, W.J. Fan, B. Long, H.B. Li, F.Y. Zhao, Z.L. Liu, Visible light Bi_2S_3 / Bi_2O_3 / $\text{Bi}_2\text{O}_2\text{CO}_3$ photocatalyst for effective degradation of organic pollutions, *Appl. Catal. B: Environ.* 185 (2016) 68–76.

[50] R.F. Liu, W.B. Li, A.Y. Peng, A facile preparation of TiO_2 /ACF with C-Ti bond and abundant hydroxyls and its enhanced photocatalytic activity for formaldehyde removal, *Appl. Surf. Sci.* 427 (2018) 608–616.

[51] C.M. Sheng, C. Wang, H.W. Wang, C.D. Jin, Q.F. Sun, S. Li, Self-photodegradation of formaldehyde under visible-light by solid wood modified via nanostructure Fe-doped WO_3 accompanied with superior dimensional stability, *J. Hazard. Mater.* 328 (2017) 127–139.

[52] M.T. Laciste, M.D.G. de Luna, N.C. Tolosa, M.C. Lu, Degradation of gaseous formaldehyde via visible light photocatalysis using multi-element doped titania nanoparticles, *Chemosphere* 182 (2017) 174–182.

[53] J.G. Yu, S.H. Wang, J.X. Low, W. Xiao, Enhanced photocatalytic performance of direct Z-scheme $\text{g-C}_3\text{N}_4$ - TiO_2 photocatalysts for the decomposition of formaldehyde in air, *Phys. Chem. Chem. Phys.* 15 (2013) 16883–16890.

[54] J. Zhou, L.F. Qin, W. Xiao, C. Zeng, N. Li, T. Lv, H. Zhu, Oriented growth of layered- MnO_2 nanosheets over $\alpha\text{-MnO}_2$ nanotubes for enhanced room-temperature HCHO oxidation, *Appl. Catal. B: Environ.* 207 (2017) 233–243.